



Ripplocations: A Progress Report

Michel W. Barsoum*

Department of Materials Science and Engineering Drexel University, Philadelphia, PA, United States

It has long been recognized that when the basal planes of crystalline layered solids were loaded edge-on in compression they failed by the formation of kink bands. And while no good model was ever put forth for how that occurred, it was always implicitly, or explicitly, assumed that basal dislocations, BDs, were the culprit. In 2015, the term ripplocation—best described as an atomic layer ripple—was coined and since then we have been making the case that atomic layers, like in other layered systems—be they playing cards, steel sheets, or geological formations—also fail by constrained buckling. In graphite, beyond a critical buckling stress, ripplocation boundaries, RBs, whose width is equal to the width of the perturbing load are formed. RBs—precursors of kink boundaries, KBs, and fully recoverable—are defined as the locus of points with the highest curvature in each layer. Once nucleated the RBs very rapidly propagate, wave-like, away from under the perturbation. Once they reach a boundary, standing waves, whose crests are RB, are formed. It is the to-and-fro motion of such waves and the concomitant friction between the layers that is responsible for the energy dissipated per cycle per unit volume outlined by stress-strain loops characteristic of layered solids that are cyclically loaded. The driving force for the reversibility of these loops is the elastic energy stored in the RBs and matrix surrounding them. Constraining motion normal to the basal planes results in an increase in buckling stresses and a decrease in the wavelengths of the resulting waves. The results of a folding mechanics model, based on confined buckling—that takes into account frictional, bending and foundation energies—on thin steel sheets not only agree surprisingly well with our experimental results, especially at low confining pressures, but also with previous work (Edmunds et al., 2006). At the atomic level transmission electron microscope, TEM, images on the MAX phases, graphite, and a layered silicate all confirm the existence of ripplocations and RBs. The existence of bulk ripplocations will require a revisiting and reassessment of our understanding of how layered crystalline solids deform.

Keywords: buckling, layered solids, ripplocations, non-linear elastic deformations, kink bands

OPEN ACCESS

Edited by:

Giles Hunt,
University of Bath, United Kingdom

Reviewed by:

M. Ahmer Wadee,
Imperial College London,
United Kingdom
Francesco Dal Corso,
University of Trento, Italy

*Correspondence:

Michel W. Barsoum
barsoumw@drexel.edu

Specialty section:

This article was submitted to
Mechanics of Materials,
a section of the journal
Frontiers in Materials

Received: 11 December 2019

Accepted: 24 April 2020

Published: 21 May 2020

Citation:

Barsoum MW (2020) Ripplocations: A
Progress Report. *Front. Mater.* 7:146.
doi: 10.3389/fmats.2020.00146

INTRODUCTION

Buckling, Kink Band Formation, and Layered Solids

Layered solids, structures and formations—in which the deformation, at least initially, is confined to two dimensions, 2D—are ubiquitous in nature and span more than 13 orders of magnitude in scale: from sub-nanometer graphene layers, to wood, laminated composites, and paperboard at the centimeter scale, to geological formations at the 100 km, or greater scale. Historically these quite different systems were studied by their respective communities with little crosstalk. More recently their commonalities have been appreciated [see (Hunt et al., 2012) and papers therein]. In these systems, buckling, kink bands, KBs, delaminations and non-linearities are common themes.

Kinking Non-linear Elasticity

It has also long been appreciated that KBs are not restricted to layered structures and formations, but also occur in layered crystalline solids, such as graphite (Kelly, 1981; Barsoum et al., 2004), mica (Bell and Wilson, 1981; Bell et al., 1986) and the $M_{n+1}AX_n$ or MAX phases (Barsoum and El-Raghy, 1999; Barsoum et al., 1999). The latter are ternary layered carbides and/or nitrides, where M is an early transition metal, A is an A-group elements (mostly groups 13 and 14) and X is C and/or N. n ranges from 1 to 4. The bonding is a combination of metallic and covalent bonding. One description of these solids is thermodynamically stable nanolaminates wherein blocks of $M_{n+1}X_n$ are separated from each other by layers of pure A.

The KBs in these solids, like for other layered formations, are most prevalent when the layers are loaded edge-on (see **Figure 4**). The MAX phases factor prominently in the history of ripplocations and it is thus worthwhile to review how they came to play such an important role. To that effect it is useful to think of them as “metals,” in which non-basal deformation is impossible. Said otherwise, only basal slip is possible.

Early on in our work on the MAX phases, it was evident that KBs were common after compressive deformation at multiple scales (**Figures 1A,B**) (El-Raghy et al., 1997; Barsoum and El-Raghy, 1999; Barsoum et al., 1999). **Figure 1C** is a scanning electron microscope, SEM, micrograph of a crack wake in a compact tension specimen. The similarity with wood, another layered solid that is prone to buckling and KB formation is obvious. These crack bridging ligaments are responsible for R-curve behavior in these solids and the relatively high fracture toughness values—(up to 15 MPa m^{1/2}) measured at room temperatures, RT, in some of them (Gilbert et al., 2000; Hu et al., 2011). From some of the micrographs (see **Figure 1D**) it was also clear that we are dealing with KB formation as a result of buckling.

In 2003, we showed that when polycrystalline MAX samples were loaded in simple compression, they outlined spontaneously and fully reversible/recoverable stress-strain loops (Barsoum et al., 2003) (**Figure 2**). We labeled such solids kinking nonlinear elastic, KNE; non-linear because the strains were non-linear and elastic because the loops were spontaneously reversible (**Figures 2A–C**). Lastly, we labeled them kinking because it was assumed/hypothesized that incipient kink bands, were responsible for KNE. Incipient kink bands—oppositely signed basal dislocation, BD, walls—were postulated in early work by Frank and Stroh (1952) on kinking in hexagonal metals.

In the intervening years, we used spherical nanoindentation, NI, experiments to show that a number of layered ceramics, such as mica (Basu and Barsoum, 2009) and graphite (Barsoum et al., 2004) were also KNE solids.

The Case Against Basal Dislocations

The central attribute of the incipient kink band idea was that it organically accounted for by the full and *spontaneous* reversibility of the stress-strain loops (**Figure 2**) by having two oppositely signed walls attract each other. However, it had several strikes against it. First and foremost, was the clear evidence for strain perpendicular to the plane of the layers, so-called c-axis strain.

The delaminations that formed upon KBs nucleation were clear and unambiguous signs of c-axis strain (**Figure 1**). The same was true of nanoindentation marks when the basal planes of some of these layered solids were loaded edge on with spherical indenters (e.g. **Figure 6A**). Basal dislocations, BDs, by definition, cannot result in c-axis strain. In retrospect, that simple observation should have been enough to rule out BDs. If this paper has a leitmotiv it is that any evidence for c-axis strain has to be due to buckling/ripplocations since it cannot be due to BDs.

We note in passing that in our zeal to explain all spontaneous stress-strain loop reversibility using incipient kink bands—the only plausible model at the time—we probably overreached. For example, in retrospect, the NI stress-strain loops observed in sapphire (Basu et al., 2006a), LiNbO₃ and LiTaO₃ (Basu et al., 2008; Anasori et al., 2011) are most probably due to reversible twin boundary motion. Conversely, those in hexagonal metals are most likely due to dislocation bowing and not incipient kink bands (Zhou et al., 2008; Griggs, 2016). Note that in hexagonal metals, KBs do form but the deformation occurs *without* delaminations, because of the activation of <c+a> dislocations (Hess and Barrett, 1949; Jillson, 1950; Gilman, 1954).

The strong anisotropy in failure stresses between tension and compression was also a clue that BDs cannot be the operative mechanism. If the driving force for deformation is shear—to nucleate and move the BDs—then, at least initially, the yield points during compression and tension should have been comparable. In layered solids they are vastly different (Budiansky et al., 1998; Narayanan and Schadler, 1999). Along the same lines, the strong influence of confining pressure on the compressive strengths of poly-, and especially single, crystals was another clue that BDs were not the operative mechanism (Kronenberg et al., 1990; Christoffersen and Kronenberg, 1993; Mares and Kronenberg, 1993). In metals, the critical resolved shear stress of dislocations, in general, and BDs in particular, is a weak function of confining pressures.

Another serious disconnect has been the one between researchers studying crystalline layered geological solids, such as micas (Bell and Wilson, 1981; Bell et al., 1986; Meike, 1989; Kronenberg et al., 1990; Christoffersen and Kronenberg, 1993; Mares and Kronenberg, 1993), where it was assumed that BDs are the operative micromechanism for deformation, and those working on geological formations that totally ignored the microscopic aspects. If BDs are important at the microstructural level, should they not also feature in the “big picture”?

To summarize this section, the fact that many crystalline layered solids fail in compression, but not tension, by forming KBs, *with delaminations*, that are quite similar to those seen in other layered systems, should have been the first clue that perhaps invoking BDs may not have been the most fruitful avenue.

RIPPLOCATIONS

A ripplocation is best described as an atomic scale ripple. The term was coined in 2015 by Kushima et al. (2015) to describe near surface defects in van der Waals solids such as MoS₂. What this paper very elegantly did was to show by density functional

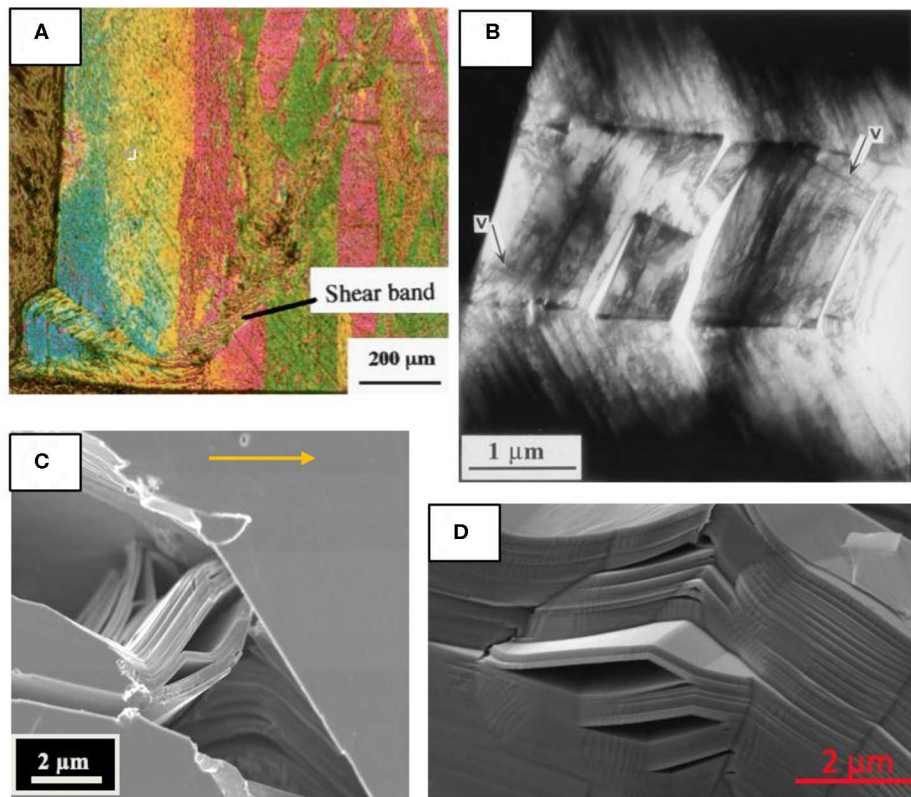


FIGURE 1 | Kink band, KB, formation in the MAX phase Ti₃SiC₂ at various scales. **(A)** Kink band formed at edge of a 2 mm cube wherein the basal planes were highly oriented vertically (Barsoum and El-Raghy, 1999). **(B)** KB in TEM, (Barsoum et al., 1999). **(C)** Field-emission scanning electron microscope, SEM, image of a bridged crack in a coarse-grained Ti₃SiC₂ microstructure (Gilbert et al., 2000). Heavily deformed lamella bridge the crack and significant amounts of delamination and bending/kinking are observed. Such processes are highly unusual in ceramic systems and account for the high plateau fracture toughness values measured. Arrow indicates direction of crack propagation. **(D)** KBs and concomitant delaminations of a solid bridge between pores (Sun et al., 2005) **(A,B)** reproduced with permission from Metallurgical and Materials Transactions A, Springer Nature. **(C,D)** Reproduced with permission from Scripta and Acta Materialia, Elsevier.

theory, DFT, and molecular dynamics, MD, calculations that same polarity surface ripplifications attracted as opposed to two same polarity dislocations that repel and are thus fundamentally different defects. That work led to the profound epiphany that ripplifications—not BDs—are the operative micromechanism in the deformation of *all* layered solids as defined herein and led to our current understanding (Gruber et al., 2016). It is important at this juncture to note that we were not the first to make the case for buckling in layered solids and formations; we are the first, however, to extend the idea to crystalline solids.

Our current understanding of ripplifications, and their properties in layered solids/systems, has accumulated, over the years, from five parallel paths: (A) Confined buckling experiments and their modeling (Edmunds et al., 2006; Barsoum et al., 2019; Badr et al., 2020); (B) Cyclic compression of polycrystalline samples (Barsoum et al., 2003; Zhou et al., 2006), (C) Nanoindentation experiments (Barsoum et al., 2004; Basu and Barsoum, 2009), (D) Transmission electron microscope, TEM, micrographs of deformed layered solids (Gruber et al., 2016; Griggs et al., 2017; Alafardov et al., 2018; Aslin et al., 2019) and, (E) MD calculations on perfect graphite single crystals at 10 degrees Kelvin, K (Gruber et al., 2016, 2020; Frieberg et al., 2018). In the remainder of this paper these five strands will be

woven together to create a ripplification tapestry that I hope is sufficiently convincing.

Confined Buckling Experiments and Their Modeling

A-1 Experimental Details

The setup we used to nucleate and model ripplifications is shown schematically in **Figure 3A** (Barsoum et al., 2019; Badr et al., 2020). This setup is similar to that used by Edmunds et al. (2006) except that in our case the foundation was not foam, but other layers and rigid fixtures on each side. We loaded the layers from the top using a cylindrical indenter, whose axis was parallel to the layers (**Figure 3A**) and captured the deformation on film. We simultaneously measured the indentation, P_N , and confining, $P_{N,0}$ loads as a function of indentation depth. To measure the latter, we embedded a load cell in one of the fixed blocks (**Figure 3A**). From these experiments the following was confirmed:

- i) The load increased more or less linearly with indentation depth up to a critical load (**Figure 3B**) at which a buckling instability occurred and standing waves below the indenter were quite rapidly formed (**Figure 3D**) (Barsoum et al., 2019;

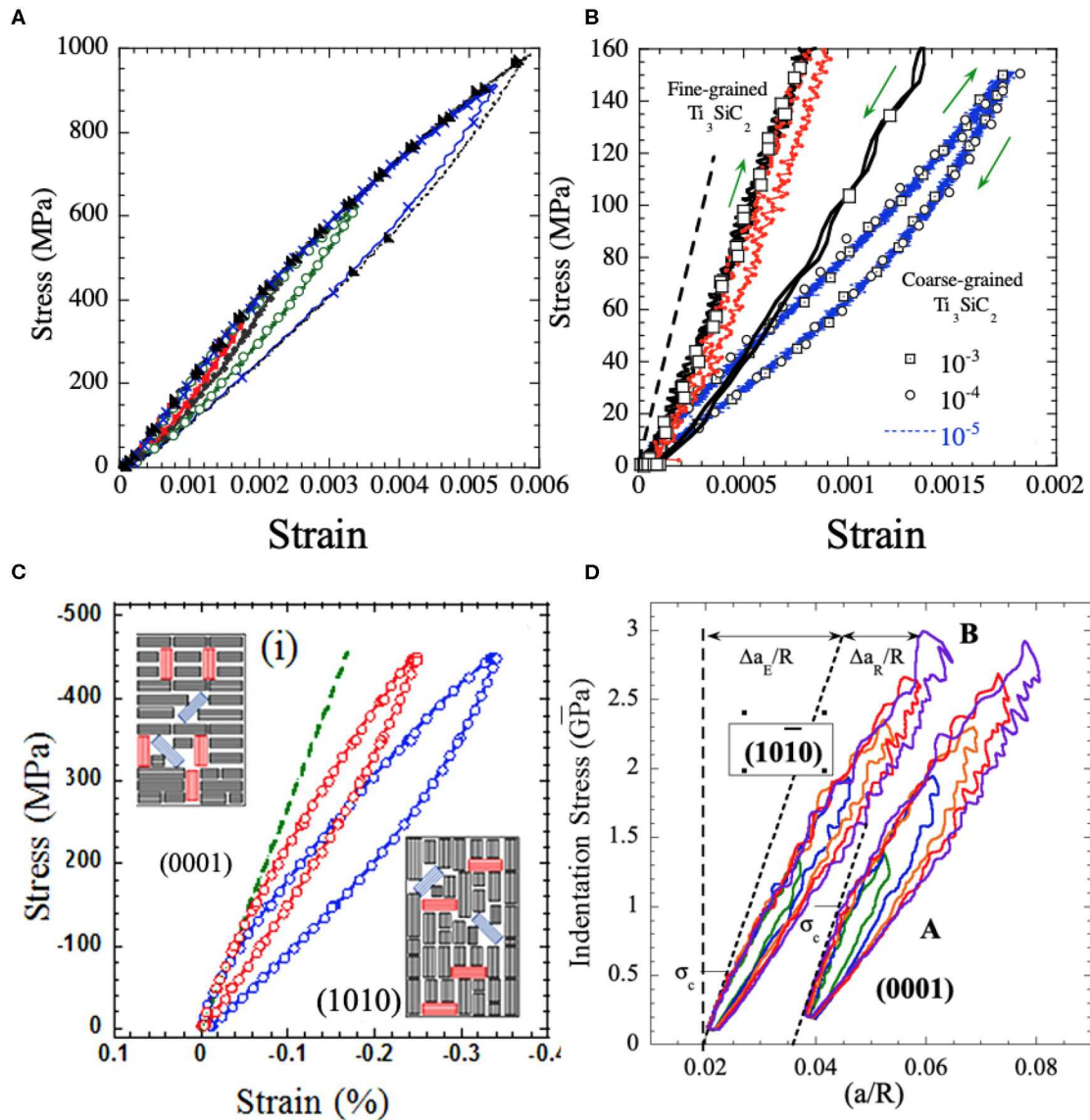
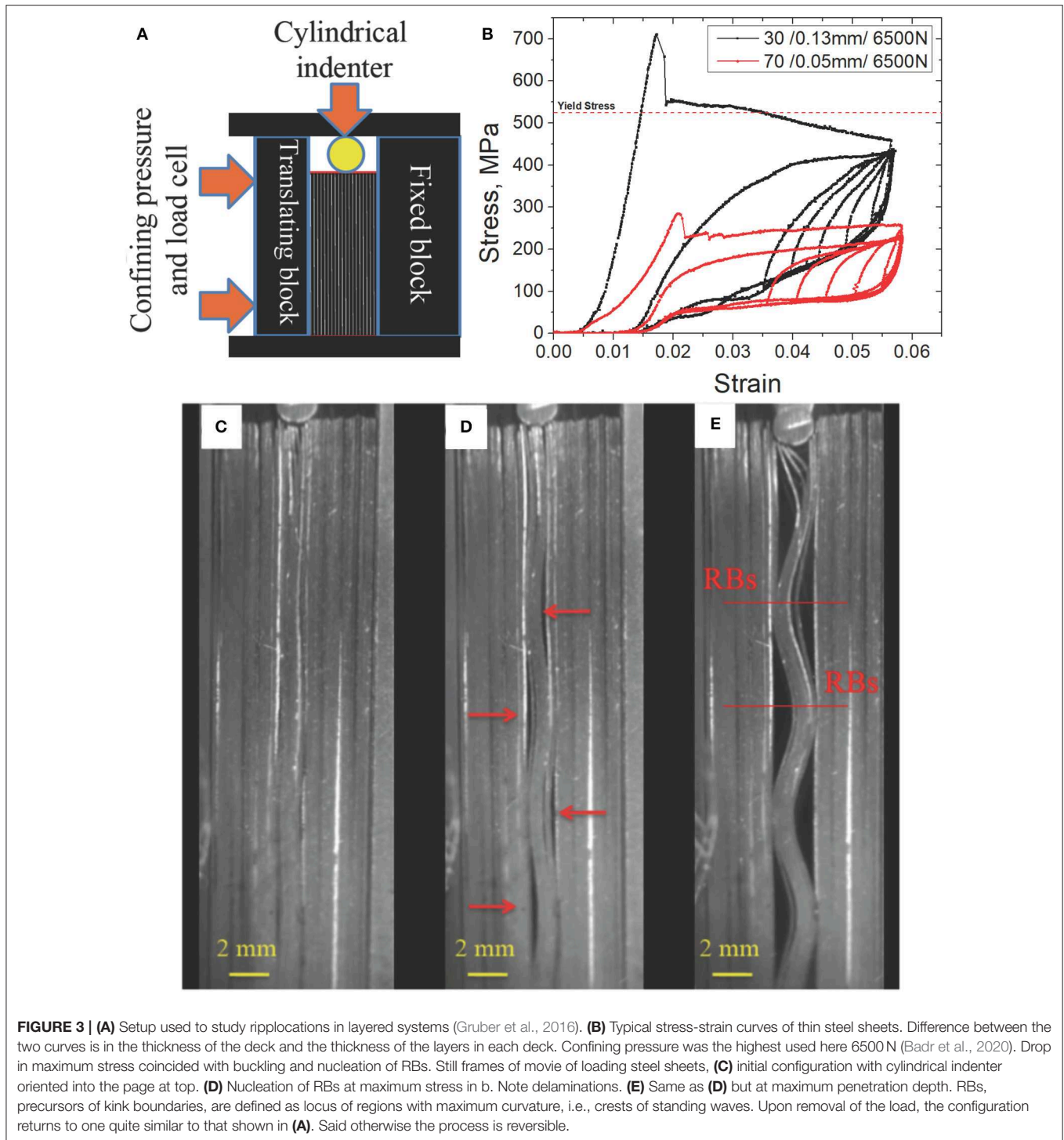


FIGURE 2 | Typical bulk cyclic compressive spontaneously reversible stress/strain loops in **(A)**, Fine-grained, FG, Ti_3SiC_2 , **(B)** Same as **(A)** but showing dramatic difference in response between coarse-grained, CG (small blue loops), and FG samples (black and red loops). Note the blue loops comprise three different loops, obtained at three strain rates indicated. Red loop—obtained on FG sample at 250 MPa—is significantly stiffer and smaller in area than the CG loops at the same stress; Within the resolution of the measurement, the three loops at the various strain rates are identical. **(C)** Highly oriented polycrystalline Ti_2AlC samples where, (i) basal planes are mostly normal to the applied load (red loop) or, (ii) parallel to the applied load (blue loop) (Shamma et al., 2015). In insets, thin lines represent basal planes. Black and red rectangles represent majority and minority hard grains, respectively. Blue rectangles represent soft grains. **(D)** NI stress vs. a/R , where a is the contact radius and R is the indenter diameter, for basal planes loaded edge on, viz. $(\bar{1}010)$ and those loaded normal to the basal planes, viz. (0001) (Griggs et al., 2017). **(C,D)** Reproduced with permission from Acta Materialia, Elsevier.

Badr et al., 2020). For reasons that are discussed below, we define a ripplaction boundary, RB, as the locus joining points the highest curvature in each layer of the standing waves (**Figure 3E**) (Frieberg et al., 2018). RBs form normal to the basal planes (**Figure 3E**) and are precursors of KBs. In contrast to KBs that are *not* reversible, RBs are (Frieberg et al., 2018).

- ii) Increasing the load, increased the amplitude of the standing waves, but not their wavelengths, λ_{RB} . $P_{\text{N},0}$ also increased linearly with indentation depth (Barsoum et al., 2019; Badr et al., 2020). The same was observed by Wadee et al. (2004) and Wadee and Edmunds (2005).
- iii) Increasing the confining, or overburden, pressure, sheet thickness, t , and/or reducing the number of layers per deck,



- increases the load at which ripplacations nucleate (e.g., **Figure 3B**) (Badr et al., 2020).
- iv) With increasing $P_{N,0}$ and t , λ_{RB} decreased (Badr et al., 2020).
- v) Upon unloading, fully recoverable, highly reproducible stress-strain loops are generated (**Figure 3B**). The driving force for the recoverability of the process is the elastic energy stored in the crests of the waves and the surrounding matrix.

- vi) Coulombic friction between the layers accounts for the energy dissipated per cycle per unit volume, W_d (Badr et al., 2020).

A-2 Mechanics Models

Because of its importance in layered systems in general, and geology in particular, the question of how layers of a

material or geological formation deform when loaded edge-on in compression is one that has been tackled by many over the years (Biot, 1964, 1965; Budiansky et al., 1998; Edmunds et al., 2006; Hunt et al., 2012). For a good overview see (Hunt et al., 2012) and references therein. The model that fits our results the best is the one by Edmunds et al. (2006).

The problem we tackle here is shown schematically in **Figure 4** and is almost identical to that of Edmunds et al. (2006) We consider n incompressible layers each of thickness, t , width, b , and height, h (**Figure 4A**) (Badr et al., 2020). If the layers have a Young's modulus, E then the bending rigidity of each layer is given by:

$$EI = \frac{Ebt^3}{12} \quad (1)$$

All buckled layers are assumed to bend about the same central line of the curvature, slip is constant between layers, and no voids are nucleated.

The applied force, P_N , is applied along h , of the layers initially confined by a force $P_{N,0}$ (**Figure 4A**). The remaining unbuckled layers, together with the rigid fixture on each side, act as the foundation and are modeled by two springs in series, each with a spring constant, k , per unit length. Experimentally, plots of the confinement force vs. displacement (not shown) were nominally straight indicating linear stiffnesses (Badr et al., 2020). Therefore, for all but one run the transverse stiffness of the foundation, c , is determined assuming

$$c = \frac{\Delta P_N}{\Delta d} = \frac{P_{N, \max} - P_{N,0}}{d_f - d_i}, \quad k = \frac{2c}{h} \quad (2)$$

where $P_{N, \max}$ is the load at maximum indentation. The horizontal deflection of the spring, Δd , is the difference between the initial, d_i , and final (viz. at maximum load), d_f , distance between the confining plates (see **Figures 4A,B**). Both are measured experimentally using image processing software and used in the model. The measured stiffness results from two springs in series and as such, k is twice c , divided by the height of layers, h . This last manipulation is performed in order to obtain a stiffness, k , per unit length.

Assuming small deformations, with a coordinate of arclength x and relatively small deflection w (**Figure 4C**), the non-linearity of the geometry is not considered dominant and is neglected. The total potential energy function, V , for this case includes the bending energy, U_B , the work done by the vertical load, U_P , the foundation energy, U_F , and the work done by friction U_μ . Working under the assumption of $T^2 \ll 4n^2 R^2 / (n-1)^2$ (i.e., that the radius of curvature R during buckling is $> T = nt$), V over a periodic half-wavelength, L , can be written as:

$$V = U_B - U_P + U_F + U_\mu$$

shown by Edmunds et al. to be:

$$V = \int_0^L \left(\frac{I}{2n^2} \ddot{w}^2 - \frac{P}{2} \dot{w}^2 + \frac{k}{2} w^2 + \frac{(n-1)\chi\mu qT}{n} |\dot{w}| \right) dx \quad (3)$$

where μ is the friction coefficient and χ is a friction indicator. When $\chi = +1$, the direction of the friction force is opposite to the external load. Conversely, when $\chi = -1$, V is negative, and the direction of the friction force is the same as the loading direction.

Using a Galerkin approximation, and assuming a deflection shape of $w(x) = A \cos(\pi x/L)$, (**Figure 4C**), where A is the wave amplitude, the linear eigenvalue analysis of V provides the critical load (Edmunds et al., 2006):

$$P_{crit} = \frac{n\pi^2 EI}{L^2} + \frac{kL^2}{\pi^2} \quad (4)$$

Minimizing the critical load with respect to the half-wavelength yields:

$$L = \pi \left(\frac{nEI}{k} \right)^{1/4} = \pi \left(\frac{nEbt^3}{12k} \right)^{1/4} \quad (5)$$

Interestingly enough neither P_{crit} nor L depend on μ . Combining Equations 1 and 5, on finds,

$$\frac{L}{t} = \pi \left(\frac{nEb}{12kt} \right)^{1/4} \quad (6)$$

It follows that a plot of L/t vs. term in brackets should yield a straight line with a slope of π .

The theoretical P_{crit} and L values determined from Equations (4) to (5), respectively, are then compared with the experimentally measured ones. Moreover, $\lambda = 2L$, and R are measured at the point of maximum indentation from the still frames. The experimental load at which buckling occurs, P_{BK} , is determined from movies taken of the sheets as they were loaded. As noted above, buckling occurs when there is a strong change in slope in the stress-strain curves.

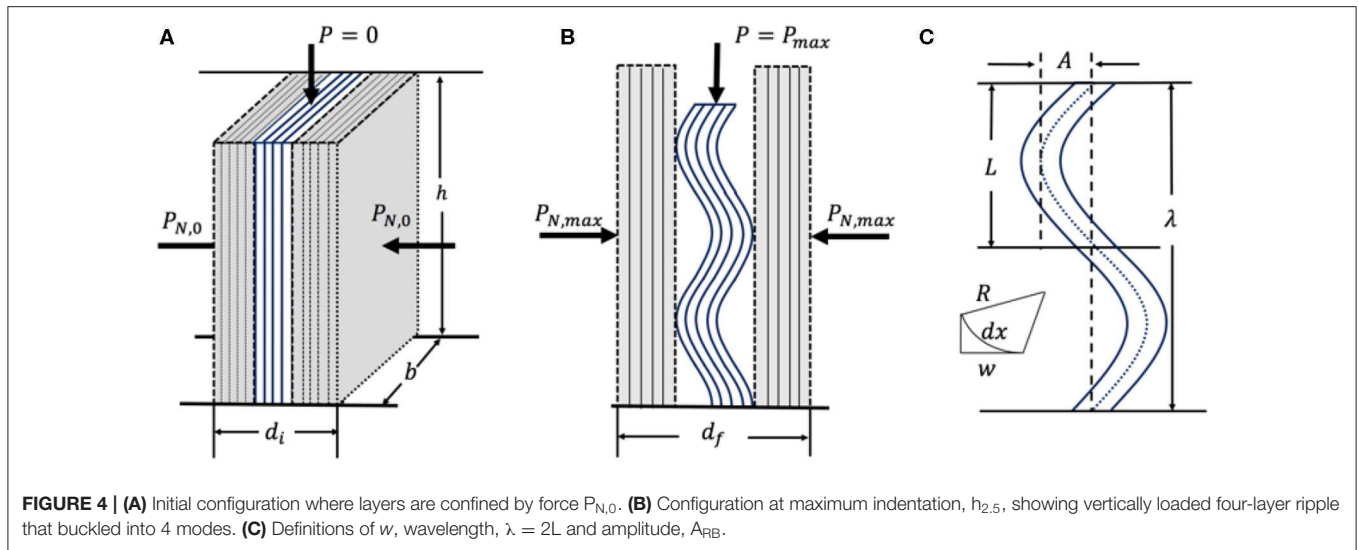
Note that the assumption,

$$T^2 \ll \frac{4n^2 R^2}{(n-1)^2}$$

where $T = nt$, works well at low confinement levels with a rigid foundation, but less at higher levels because the curvatures decrease to the order of, or less than, the overall thickness of the buckled layers. As a result, we introduce the term:

$$\eta = \frac{4n^2 R^2}{(n-1)^2 T^2}$$

which is essentially a non-dimensionalized ratio of the curvature and overall thickness of the buckled layers as an indicator of how well the aforementioned inequality holds. The higher the value of η , the better the model predictions and experiments align. In other words, agreement between theory, and experiment should be best at large values of η and become increasingly less so at high levels of confinement, i.e., for $\eta < 20$. Similar arguments were made in Budd et al. (2003) and Edmunds et al. (2010).



A-3 Energy Dissipated per Cycle

Intriguingly, as noted above, neither P_{crit} nor L depend on μ . That cannot be true of the energy dissipated per cycle per unit volume, W_d . All the nested loops shown in **Figure 2B**, are fully recoverable. Under these conditions, and further assuming, $\sigma_{RB} \approx 2\tau_{RB}$, the following relationship is approximately valid:

$$W_d = 2 \tau_{RB} \gamma_{RB} \approx (1 + \nu) \sigma_{RB} \epsilon_{RB} \quad (7)$$

where γ_{RB} , ϵ_{RB} and ν are the applied shear and normal strains and Poisson's ratio, respectively. τ_{RB} and σ_{RB} are the shear and normal stresses needed to move the RBs. If we further assume Coulombic friction, viz. $P_S = \mu P_N$, where P_N and P_S are the average loads acting normal and parallel to the layers during a cycle, it follows that (Badr et al., 2020):

$$W_d = (1 + \nu)\mu \frac{P_N \epsilon_{RB}}{A_{ind}} \quad (8)$$

If this equation is valid, and μ is not a function of P_N , then plots of W_d vs. $(P_N \times \epsilon_{RB})/A_{ind}$ should yield straight lines with slopes equal to $\mu(1+\nu)$. Here, A_{ind} is indented area.

A-4 Critical Analysis of Model

Figure 5A compares, on the same plot, the predicted and experimentally determined λ_{RB} values for thin steel plates (Badr et al., 2020) and paper (Edmunds et al., 2006). Going one step further, Equation 6 predicts that a plot of L/t vs. the term in brackets should yield a straight line with a slope of π . **Figure 5B** combines our results on steel and those of Edmunds et al. (2006) on paper. A least square fits of both sets of results yields a slope of 3.21 and an R^2 value of 0.957. This overall agreement has to be considered excellent given the very large differences in experimental setups—solid foundation with large overpressures vs. foam—and the materials tested; steel vs. paper.

Figure 5C compares the theoretical and experimental buckling stresses for our and Edmunds et al. (2006) results. Based on these results it is reasonable to conclude that the

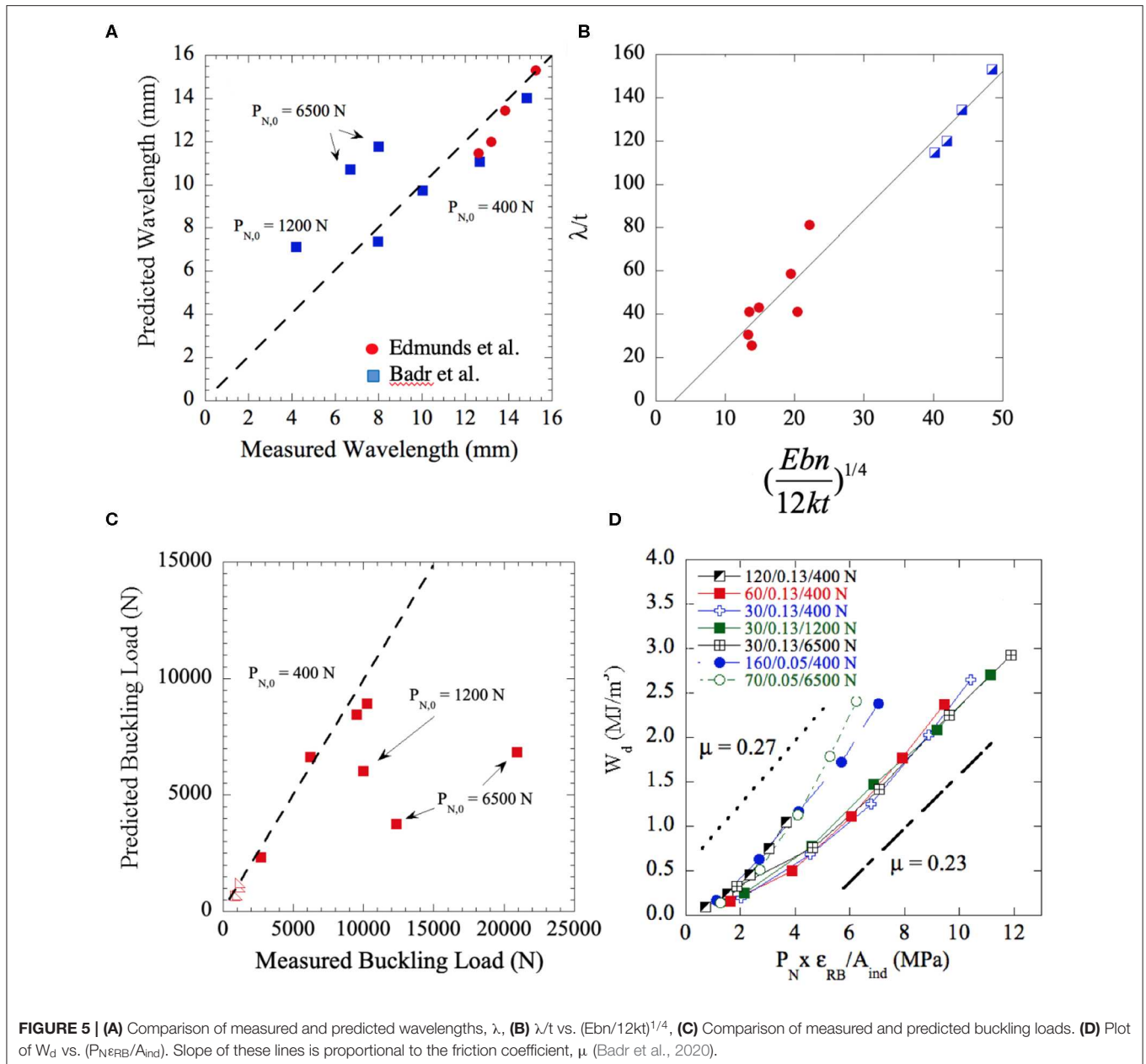
Edmunds et al. model is quite accurate for predicting the wavelengths of RBs and their buckling stresses. Note that the agreement in the steel case is less good for large confinement stresses (1,200 and 6,500 N). In that regime $T^2 \ll \frac{4n^2 R^2}{(n-1)^2}$ is no longer valid.

According to Equation 8, if μ is not a function of P_N , then plots of W_d vs. $(P_N \times \epsilon_{RB})/A_{ind}$ should yield straight lines with slopes equal to $\mu(1+\nu)$. **Figure 5D** shows that to indeed be the case. The second row of **Table 1** lists the values of μ assuming $\nu = 0.3$ and the slopes of the lines plotted in **Figure 5D**. Given the simplicity of the model used to derive Equation 7, the results shown in **Figure 5D** are quite gratifying for several reasons:

- i) Coincidentally or not, the μ values listed in the last row in **Table 1**, averaging 0.23 ± 0.03 , are in excellent agreement with the experimentally measured μ values of 0.23 and 0.27 for the thick and thin sheets, respectively. This agreement lends credence to our experiments, analysis and simple model (Badr et al., 2020).
- ii) This in turn implies that Coulombic friction, viz. $P_S = \mu P_N$, is applicable and that μ is not a strong function of P_N . The curvature seen in the curves, however, suggest, not too surprisingly, that μ may not be totally independent of $P_{N,0}$.
- iii) Lastly the results plotted in **Figure 5D**, show that a straightforward method to increase W_d is to start with thinner sheets (top curves in **Figure 5D**).

Cyclic Compression of Polycrystalline Samples

As noted in the introduction, we have shown, over the years, that when polycrystalline MAX phase samples were cyclically loaded in simple compression, fully recoverable, stress-strain loops were obtained (**Figure 2**). We labeled such solids KNE. The latter share the following characteristics:



- i) The initial slopes of the stress-strain curves are linear and equal to the elastic moduli of the materials being tested. The dashed oriented lines in **Figures 2B,C** and **d** are what would be expected if no kinking occurred. With increasing stress, the response becomes non-linear. The stress at which the nonlinearity is observed—the kinking or buckling stress—is a strong function of grain size, with smaller grains being much more resistant to buckling (**Figure 2B**).
- ii) When cycled, fully recoverable stress-strain loops are obtained. The shape and size of the loops are *not* a function of strain rate, at least in the 10^{-5} to 10^{-3} s^{-1} range in Ti_3SiC_2 deformed at RT (**Figure 2B**) (Barsoum et al., 2003).
- iii) W_d is larger, on an *absolute* scale, for 10 % porous Ti_2AlC MAX samples, than for their fully dense counterparts (Zhou et al., 2006). This result is fully consistent with buckling.
- iv) When highly oriented polycrystalline Ti_2AlC samples were compressed, W_d for samples where the basal planes were loaded edge-on were higher than those in which the load was along the c-axis (**Figure 2C**) (Shamma et al., 2015). The latter microstructure/loading will be referred as (0001), while the former will be referred to as (0 $\bar{1}$ 01).
- v) The kinking nucleation stresses were higher for (0001) than for (0 $\bar{1}$ 01) samples.
- vi) W_d is a strong function of grain size (**Figure 2B**). W_d in tension is at least an order of magnitude smaller than in

compression (Radovic et al., 2000). The same is true of the failure stresses.

- vii) At higher temperatures, the response becomes time dependent. The loops are larger and are a function of strain rate. Cyclic hardening is observed at temperatures as high as 1,200°C in air Zhen et al. (2005a) and Barsoum et al. (2003).
- viii) Cyclic hardening, at room temperature, RT, is observed after small deformations at higher

temperatures (Zhen et al., 2005b). This results from a grain size refinement of the microstructure. This refinement is due to the formation of multiple kink boundaries/bands.

- xi) TEM micrographs of post-crept samples show low defect concentrations suggesting that the grain boundaries are potent sinks of RBs at higher temperatures (Barcelo et al., 2010).

TABLE 1 | Least squares of slopes of lines shown in **Figure 5D**.

Exp. setup	120/1.3/400	60/1.3/400	30/1.3/400	30/1.3/1200	30/1.3/6500	70/0.05/6500	160/0.05/400
Slope	0.278 [‡]	0.284	0.285	0.28	0.283	0.33 [‡]	0.35 [‡]
μ	0.209	0.236	0.239	0.219	0.231	0.236	0.303

The μ values are calculated assuming $\nu = 0.3$. The first number in the top row designate number of sheets, the second their thickness in mm and the third is the initial confining pressure in N, applied to the stacks. [‡]Only first 3 points in **Figure 5D**, were used to calculate these values since beyond these points the curves are non-linear and all our assumptions are for a linear system. Last row lists the calculated friction coefficients.

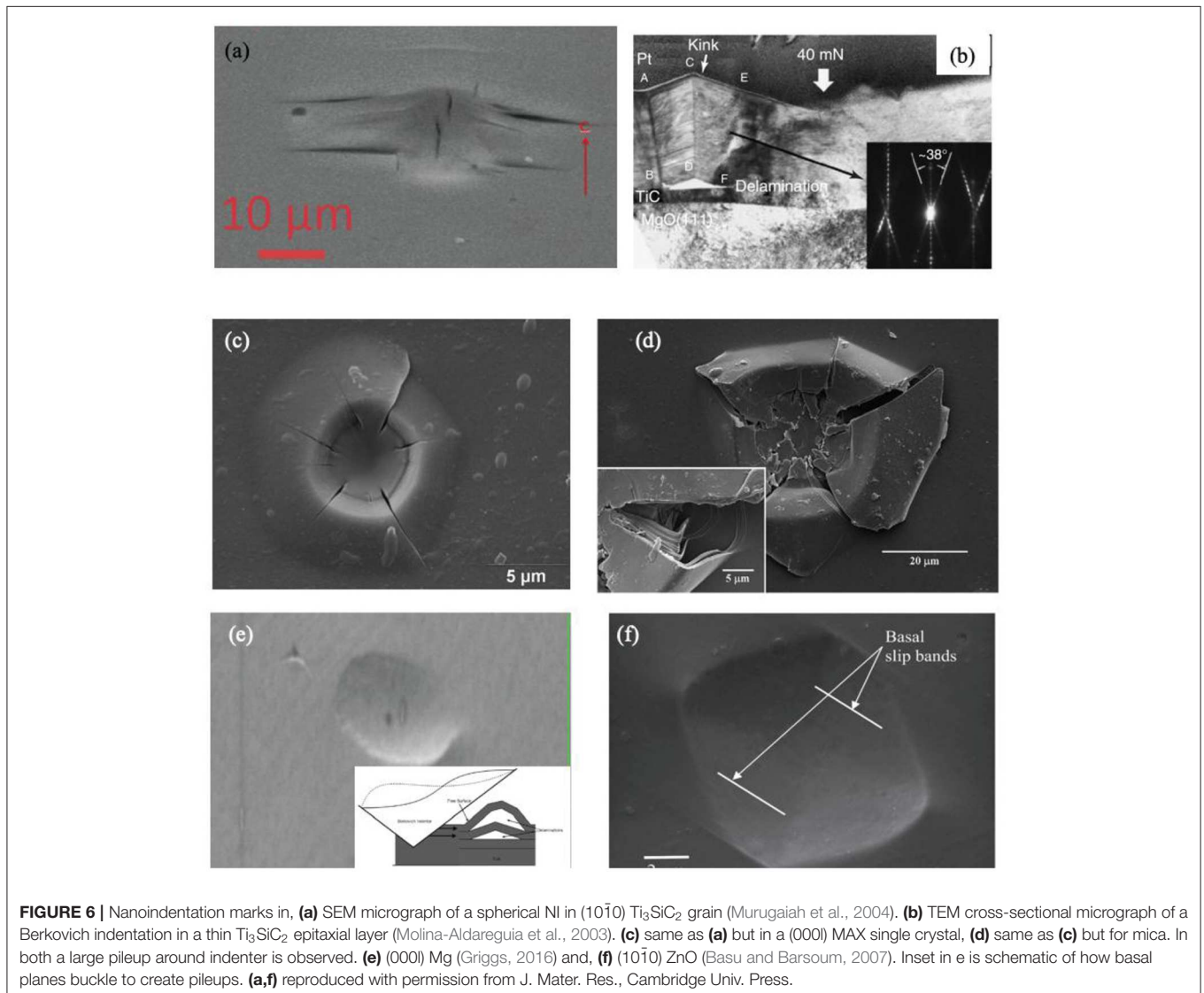


FIGURE 6 | Nanoindentation marks in, **(a)** SEM micrograph of a spherical NI in $(10\bar{1}0)$ Ti_3SiC_2 grain (Murugaiah et al., 2004). **(b)** TEM cross-sectional micrograph of a Berkovich indentation in a thin Ti_3SiC_2 epitaxial layer (Molina-Aldareguia et al., 2003). **(c)** same as **(a)** but in a (0001) MAX single crystal, **(d)** same as **(c)** but for mica. In both a large pileup around indenter is observed. **(e)** (0001) Mg (Griggs, 2016) and, **(f)** $(10\bar{1}0)$ ZnO (Basu and Barsoum, 2007). Inset in e is schematic of how basal planes buckle to create pileups. **(a,f)** reproduced with permission from J. Mater. Res., Cambridge Univ. Press.

As noted in the introduction, the full spontaneous reversibility was previously ascribed to the attraction of two oppositely signed dislocation walls comprising the IKBs (Barsoum et al., 2005). Based on the results shown in this and following sections, it is now obvious that the origin of the reversibility is much more mundane and due to the elastic energy stored in the system—both in the crests of the RBs standing waves and the surrounding matrix—during loading.

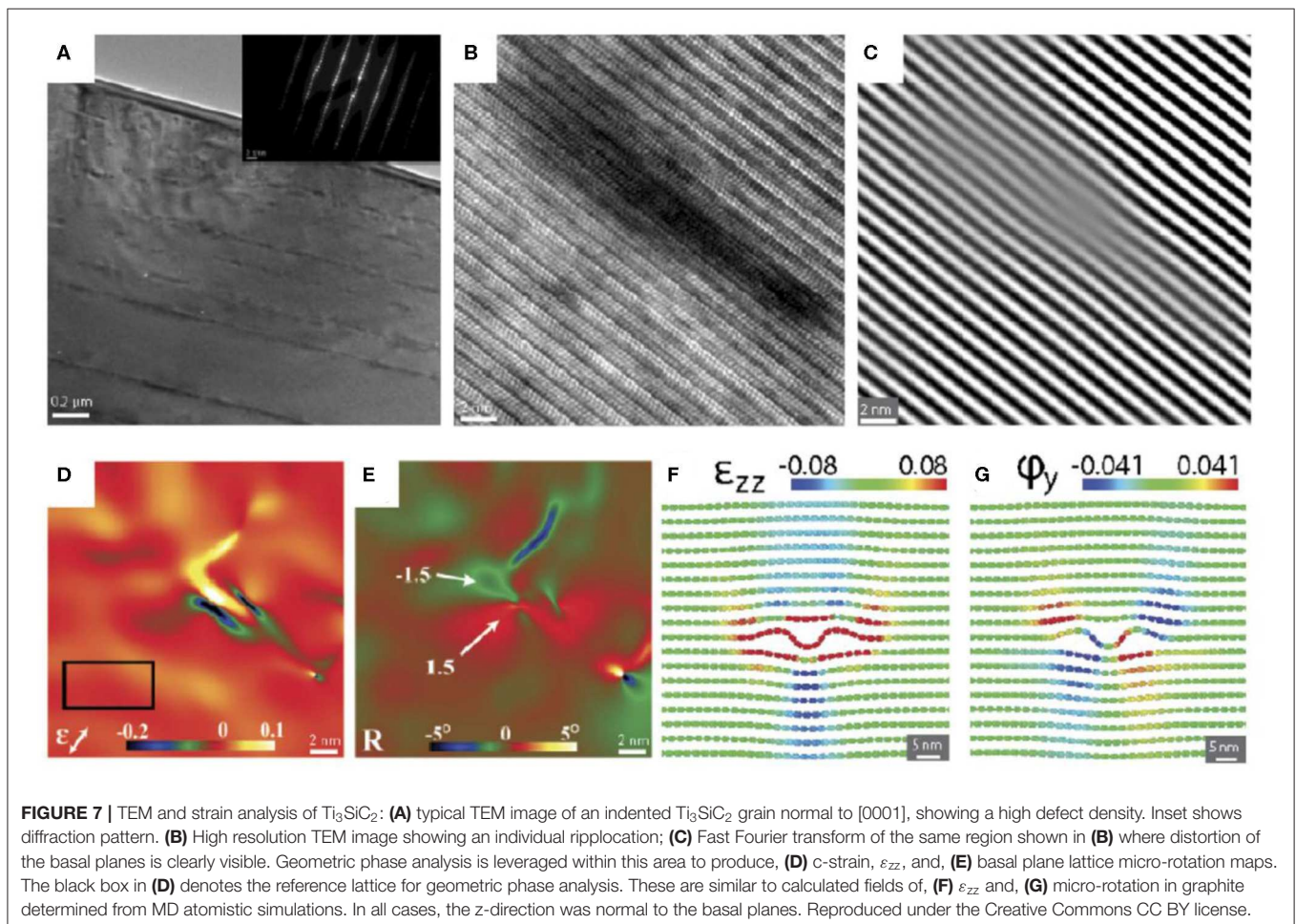
Nanoindentation Experiments

After the MAX phases were classified as KNE solids, the question that arose was how to prove it in materials, like layered ceramics, that were more brittle. Here we turned to nanoindentation, NI, experiments on mostly ceramic single crystals (Basu and Barsoum, 2009). To obtain stress/strain curves we used spherical indenters of varying radii, R , and developed a methodology to convert the NI load-displacement curves to NI stress, σ_{NI} . We then plotted σ_{NI} vs. a/R plots (Basu et al., 2006b; Moseson et al., 2008). Typical plots for two orientations of Ti_3SiC_2 grains [(0001) and (0101)] are shown in **Figure 2D**. In most cases, the indenter was thrust into the *same* location, sometimes as many times as 50 times, before nested loops such as those shown in **Figure 2D**,

were generated, and analyzed (Griggs et al., 2017). Note similarity between **Figures 2A,D**.

Based on the totality of our results the following has been established:

- i) For the most part, during the first cycle, the response is linear elastic, with a slope proportional to the elastic modulus of the surface being indented (Basu and Barsoum, 2009; Griggs et al., 2017). In some cases, this linearity was followed by large pop-ins. The latter were more frequent in the (0001) orientation and when the pop-in stresses were high (Barsoum et al., 2004; Basu and Barsoum, 2009; Griggs et al., 2017). In one case, a 60 μm pop-in was observed in a (0001) single crystal of graphite (Barsoum et al., 2004). In the (0101) orientation, the extent of the pop-ins and the stresses at which they occurred were significantly smaller (Griggs et al., 2017).
- ii) During most first cycles, a permanent deformation is observed. In the absence of this deformation, the response is, for the most part, linear elastic.
- iii) When they could be compared, the buckling stresses were significantly lower in (0101) grains than their (0001) counterparts (Griggs et al., 2017). This is not too surprising



since intuitively it is easier to buckle grains when their basal planes are loaded edge-on ($0\bar{1}01$), than normal to them, i.e., along the c -axis.

- iv) In contrast to when polycrystalline samples were loaded, W_d was smaller in the ($0\bar{1}01$) grains than the (0001) ones (**Figure 2D**) (Griggs et al., 2017).
- v) Consistent with the need of the basal planes to expand upon the introduction of BRs, the initial friction stress needed to nucleate and move them was found to be almost three times lower when the basal planes are loaded edge-on (Griggs et al., 2017).

Here again, the most compelling and straightforward evidence for ripplacation nucleation and movement under various indenters is the c -axis strain observed. The latter is manifested in two ways depending on the orientation of the basal planes relative to the indentation direction. When ($0\bar{1}01$) planes are loaded, delamination cracks (**Figure 6a**) are formed. Such cracks are strong evidence for buckling since they *cannot* be explained

by the nucleation and movement of BDs alone. In the (0001) case, large buildup/pileup of material at the indentation edges is the evidence needed to conclude that BDs alone, cannot be the culprit (**Figures 6b–d**). This large buildup is a result of the buckling of near-surface layers due to the thrust of the indenter into the material. In this orientation, what is occurring is shown schematically in inset of **Figure 6e** (Kooi et al., 2003). As the nanoindenter is pushed into the surface, the basal planes buckle out of the surface plane and end up as large pileups near the indentation marks as shown nicely in **Figures 6e,f**.

These observations are important for another reason; they are clear evidence that RB are responsible. In crystalline solids, in which $\langle c+a \rangle$ dislocations can be nucleated under the indenter, the indentation mark is “metallurgical” in character, in that neither a large pileup of material nor delamination cracks (**Figure 6e**)—even in a brittle material such as ZnO (**Figure 6f**) (Basu and Barsoum, 2007)—are observed. Said otherwise, large pileups and delamination cracks are characteristics of ripplacations. It follows that a simple method to determine

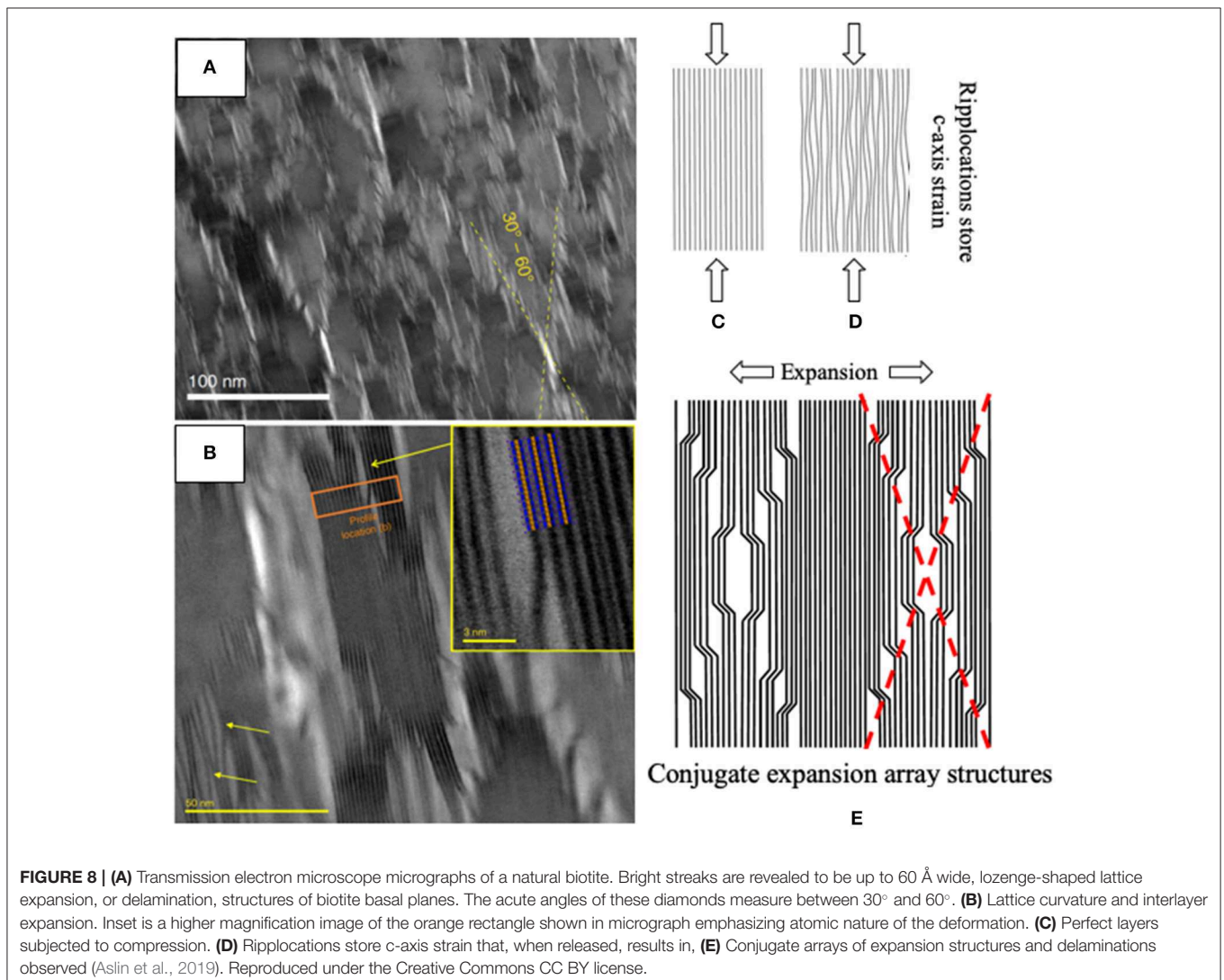


FIGURE 8 | (A) Transmission electron microscope micrographs of a natural biotite. Bright streaks are revealed to be up to 60 Å wide, lozenge-shaped lattice expansion, or delamination, structures of biotite basal planes. The acute angles of these diamonds measure between 30° and 60°. **(B)** Lattice curvature and interlayer expansion. Inset is a higher magnification image of the orange rectangle shown in micrograph emphasizing atomic nature of the deformation. **(C)** Perfect layers subjected to compression. **(D)** Ripplacations store c -axis strain that, when released, results in, **(E)** Conjugate arrays of expansion structures and delaminations observed (Aslin et al., 2019). Reproduced under the Creative Commons CC BY license.

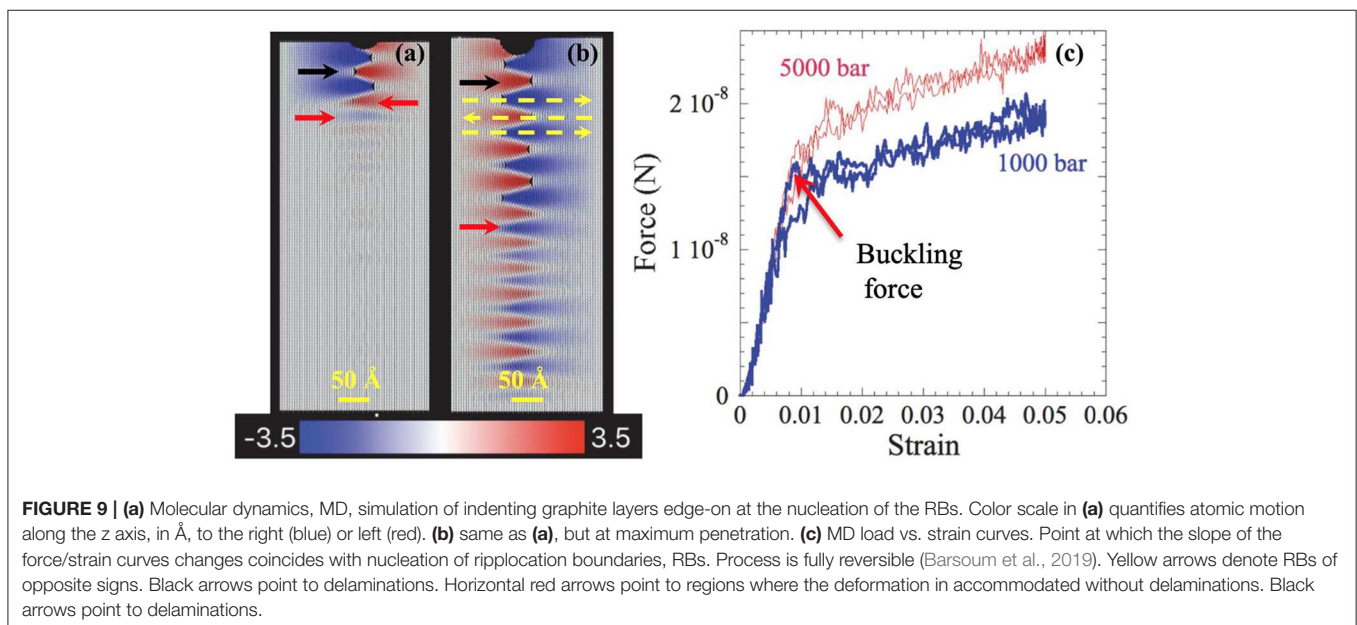
whether a material deforms by ripplocations is to carry out spherical NI experiments normal to and/or parallel to the basal planes.

It is important to stress here that if the applied NI stress is lower than that needed to nucleate permanent KBs (see below), there is typically little trace of the indentation. The response, however, is not linearly elastic since considerable energy is dissipated during each cycle.

Transmission Electron Microscopy of Deformed Layered Solids

In the following, we summarize ours, and others', TEM work on deformed layered solids.

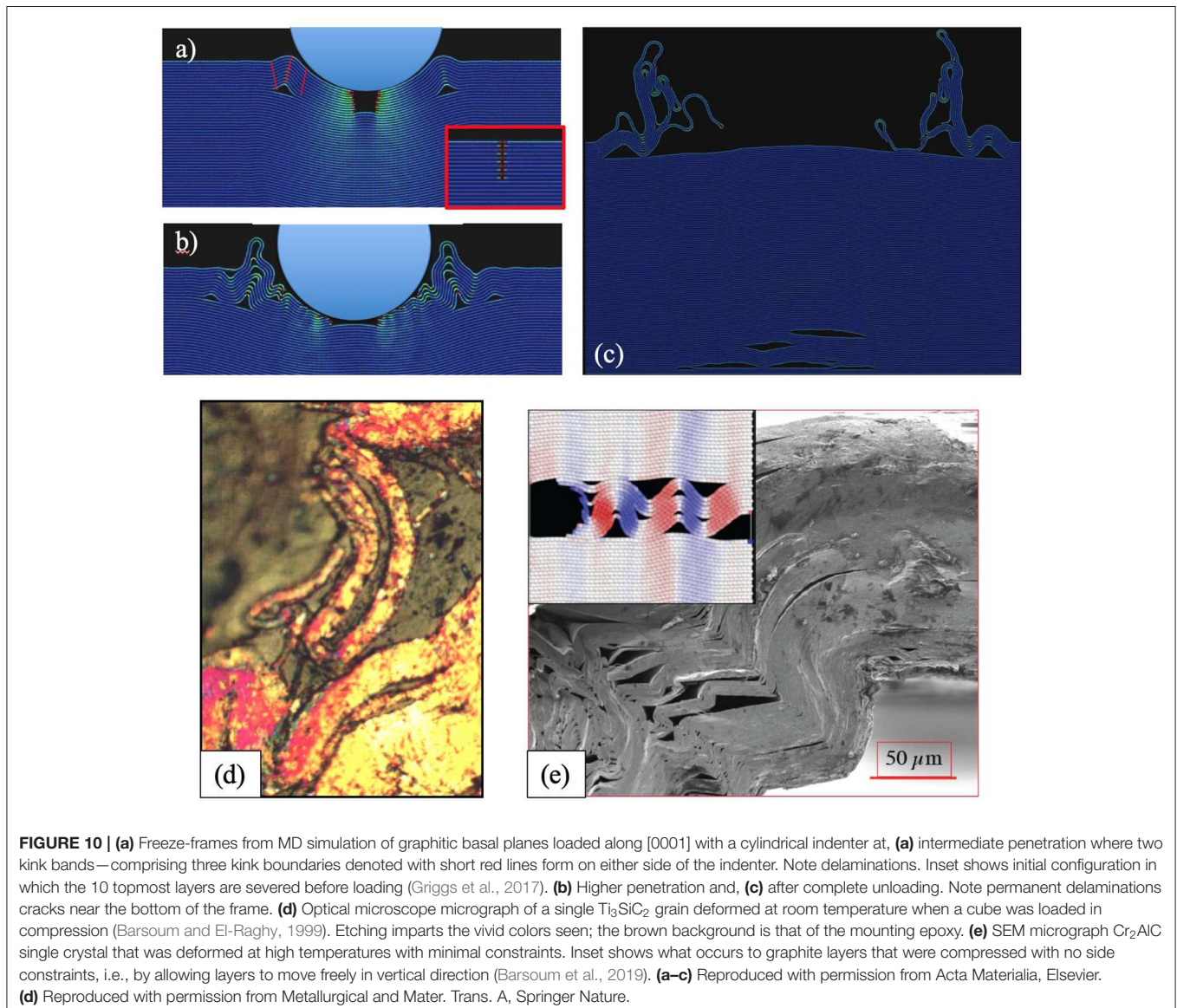
- i) Kushima et al. showed direct evidence for ripplocations in MoS₂ (Kushima et al., 2015). They also directly observed ripplocation generation, and motion, when few-layer MoS₂ films were either lithiated or *in situ* loaded in the TEM.
 - ii) In the MAX phases, ripplocations in the TEM manifest themselves as dark streaks parallel to the basal planes (**Figures 7A,B**) (Gruber et al., 2016; Griggs et al., 2017). Crucially, geometric phase analysis of these features showed evidence for c-axis strain that was similar to our MD simulations of ripplocations in graphite (**Figures 7D–G**) (Gruber et al., 2016; Griggs et al., 2017). Since c-axis strain is impossible for BDs, the streaks have to be due to something else. Fast Fourier transforms of these features resulted in the observation of undulating basal planes that can be described as ripplocations (**Figure 7C**) (Gruber et al., 2016; Griggs et al., 2017).
 - iii) In a study on post-neutron irradiation defects in the MAX phases, we presented evidence for two types of defects: interstitial dislocation loops for which a $g \cdot b$ condition was found that rendered them invisible and another set for
- iv) Kabiri et al. *in situ* deformed the MAX phase, Nb₂AlC, both normal, and parallel, to the basal planes in a TEM (Kabiri et al., 2017). And while they concluded that BDs were the operative micromechanism, their results—critically the anisotropy observed—only make sense in a ripplocation framework. In that work, the reversibility of the process was also nicely demonstrated.
 - v) Alaferdov et al. presented TEM evidence of ripplocations in graphite nanoplatelets after sonication (Alaferdov et al., 2018).
 - vi) Nano-scale bending features or nanobridges (**Figures 8A,B**)—that *cannot* be explained by BDs alone—were ubiquitous in biotite grains (Aslin et al., 2019). These features created conjugate delamination array structures that are the result of elastic strain energy release due to the accumulation of layer-normal, or c-axis strain, due to the presence of ripplocations (see **Figures 8C–E**). This explains why the diamond-shaped expansional arrays are crystallographically controlled as evidenced by the fact that they have different orientations in different grains. In all cases, however, the arrays were aligned *normal* to the c-axis of each grain (**Figures 8A,B**). Conjugate delamination arrays represent the most efficient way to relieve stored grain-scale c-axis strain energy, just as conjugate normal faults result from extension on a larger scale. The orientations of



principal stresses in this figure are therefore representative of the time when stored elastic strain energy is released (most probably during thinning the samples for TEM observation), and not necessarily the time during which the strain was being accumulated, i.e., in the geological formation they were found.

To summarize this section, direct, and indirect, TEM evidence of RBs and features—like nanobridges and conjugate arrays of expansion—that can only be explained by the presence of ripplocations exist. The importance of the biotite work cannot be overemphasized since it is the first to present direct evidence for ripplocations and RBs in an important geological material. BR provide the missing mechanism necessary to understand phyllosilicate deformation, with important rheological implications for phyllosilicate bearing seismogenic faults and subduction zones.

In the past, delaminations and hysteresis in weakly bonded geological materials were assumed to be due to fast fracture and concomitant delaminations. And while this may be true of non-layered solids, (Walsh, 1965; David et al., 2012) this claim has to be carefully scrutinized in case of layered solids. For example, the results shown in **Figure 8**, belie this notion since, at least in this material, the delaminations were due to *c*-axis expansions. Said otherwise, in some cases, the cracks and delaminations are due to ripplocations. The distinction is important: In the brittle case, the cracks would extend across the entire sample or formation, in the other, the deformed region hardens which then results in more delaminations and ultimately conjugate arrays (**Figure 8**). *In short, conjugate delamination array structures in layered solids are clear evidence of the release of c-axis strain associated with ripplocations and RBs.*



Lastly in this section it is important to note that direct TEM evidence for ripplocations in graphite have long existed. The features observed were not labeled as such, however (Muto and Tanabe, 1999; Asthana et al., 2005; Eapen et al., 2014).

MD Simulations

The following applies to bulk ripplocations in graphite at 10 K. A straightforward method to nucleate ripplocations is to add carbon atoms to a given graphitic basal plane (Kushima et al., 2015; Gruber et al., 2016). Based on our work and that of others, it is more or less established that:

- i) Ripplocations nucleate as a result of buckling. In the bulk, the buckling is confined (Gruber et al., 2016). At, or near, surfaces it is unconfined (Kushima et al., 2015). Ripplocation nucleation results in a clear change in the slope of the force vs. strain curves (**Figure 9c**).
- ii) The process is almost fully reversible/recoverable and removal of the indenter results in a pristine sample. The areas of the stress-strain loops are quite small, however compared to those measured in our macroscopic experiments. These areas, for reasons that are not clear at this time, are a strong function of strain rates (Barsoum et al., 2019). More work is needed to understand this intriguing result.
- iii) Once nucleated BRs, whose extent is equal to the size of the indenting surface, very rapidly propagate like waves away from under the indenter (**Figure 9a**). Upon reaching a boundary, standing waves arise (**Figure 9b**). As noted above, the locus of points joining the highest curvature in each layer of the standing waves was termed a RB. These are shown as dotted yellow lines in **Figure 9b** and are similar to those observed in **Figure 3C** (Frieberg et al., 2018).
- iv) BRs are attracted to each other regardless of their polarity (Gruber et al., 2016). A single ripplocation, like a dislocation interstitial loop has no Burgers vector (Gruber et al., 2016). A single ripplocation, like a single dislocation is scientifically interesting, but of limited utility. In graphite, ripplocations are attracted to other ripplocations, both within the same layer and on adjacent layers. Interestingly enough, single surface ripplocations act as solitons (Savin et al., 2019).
- v) As noted above, the critical distinction between a KB and RB is that while the latter is fully reversible, the former is not.
- vi) When the radii of curvatures of the RBs are no longer sustainable, they transform to the ubiquitous and well-established KBs. Once a KB forms (not shown), the system is “broken” and no-longer fully reversible.
- vii) BRs can only nucleate at free surfaces. Nucleating a BR in solids entails severing/cutting atomic planes. Once severed, the two free ends of the basal planes can move in opposite directions (Griggs et al., 2017). Ripplocations spontaneously also migrate away from remote compressive stresses (Gruber et al., 2020).
- viii) In graphite, even at 10 K, ripplocations are quite mobile indeed and are attracted to vacancies (Gruber et al., 2020). The energy needed to move them is a function of their widths, but asymptotically reach ≈ 32 meV.

To understand RB nucleation, we cyclically loaded, *in silico*, the basal planes of graphite single crystals edge-on with cylinders of radii of 50, 100, and 250 nm (Frieberg et al., 2018). The response was initially linear elastic, followed by the nucleation and growth of multiple, fully reversible RBs below the indenter. The RBs that nucleate from the alignment of ripplocations on adjacent layers

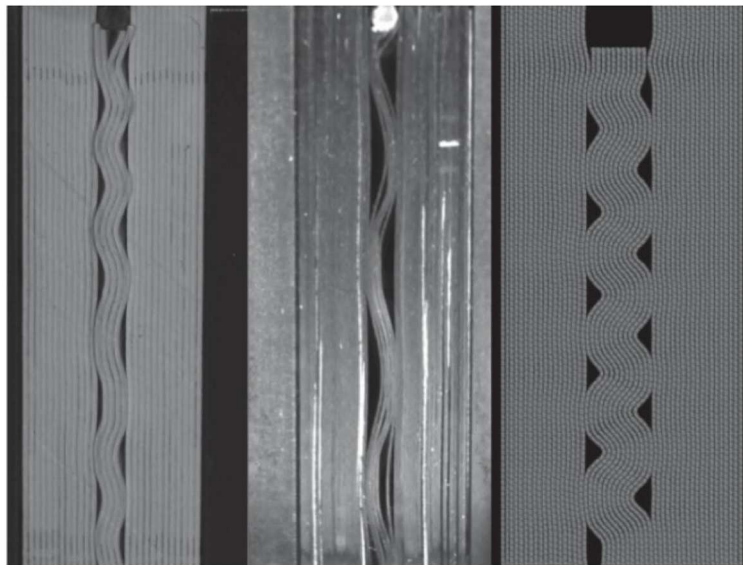


FIGURE 11 | Snapshots of RBs formed when a cylindrical indenter is loaded edge-on into plastic cards (**left**), thin steel plates (**middle**), and graphite (**right**). The latter is a result of a MD simulation. The scales are intentionally not shown.

are exceedingly non-local and propagate, wavelike, away from the indented surface. As importantly, and consistent with buckling, because the number of atomic columns loaded under the 50 nm indenter are fewer than the ones that form under the 250 nm indenter, they nucleated at lower stresses (Frieberg et al., 2018).

We also carried out molecular dynamics simulations on graphite at 10 K and faithfully reproduced many features observed below indenters in Ti_3SiC_2 . Here we give three examples. In **Figures 10a,b**, we indented a (0001) surface with a spherical NI. At low penetrations (**Figure 10a**), how the basal planes buckle out of the way is obvious. The similarities between **Figure 10a** and say **Figure 6b** should be clear at this time. At higher penetrations (**Figure 10b**) the buckling becomes much more complicated. At maximum penetration the regions next to the indenter look quite unusual indeed (**Figure 10c**). Such structures would seem fantastical had they not been directly observed (**Figure 10d**) near the buckled corner shown in **Figure 1A**, where small Ti_3SiC_2 cubes were deformed (Barsoum and El-Raghy, 1999). Lastly, **Figure 10e**, shows a SEM micrograph of a Cr_2AlC single crystal that was deformed at high temperatures. That the basal planes buckled is clear. The inset in **Figure 10e** is a MD simulation of graphite in which the basal planes were loaded edge-on without constraining the sides (i.e., deformation is allowed along the vertical direction). The similarities between the simulation and the deformed sample is quite striking given the orders of magnitude differences in scale and bonding between the two materials. There is also little doubt that the deformation mode observed is one due to compressive buckling and *not shear*. Indeed, it would be very difficult, if not impossible, to explain these micrographs in a shear-based universe.

SUMMARY AND CONCLUSIONS

The atomic planes in crystalline solids, like other layered systems or formations, buckle when loaded in compression. The micromechanism responsible for the buckling is a ripplocation. Ripplocations in graphite are attracted to vacancies and to each other, regardless of their polarity. They are also quite mobile even at 10 K in graphite. When a few layers of graphite are loaded

with a cylindrical indenter, the response is initially linear elastic. At a critical buckling stress, multiple ripplocation boundaries, RBs, are nucleated. Once nucleated, these RBs—whose width or breadth is equal to that of the indenter used—very rapidly propagate, wave-like, away from under indenter and result in standing waves, the crests of which we labeled RBs.

It is the to-and-fro motion of RBs and the concomitant friction that is responsible for the dissipated energies when layered solids are cycled. The elastic energy stored in the crests of the RBs and surrounding matrices is responsible for the near full reversibility or recoverability of the process.

Lastly, **Figure 11**, reproduces the RBs that form when playing cards, thin steel sheets and graphite single crystals are loaded edge on. No micron markers are shown to emphasize the self-similarities of these features that span ≈ 9 orders of magnitude in scale. The existence of bulk ripplocations and ripplocation boundaries, will require a revisiting and reassessment of our understanding of how layered crystalline solids deform.

AUTHOR CONTRIBUTIONS

The author confirms being the sole contributor of this work and has approved it for publication.

FUNDING

CMMI division of NSF funded this work (grant number 1728041). The budget did not include publication fees.

ACKNOWLEDGMENTS

This work would not have been possible without my colleagues, G. Tucker and L. Lamberson, who are now at the Colorado School of Mines, CO, who developed the MD simulations of graphite and the mechanics model, respectively. Without their crucial contributions to the problem our understanding of ripplocations would not have come as far as it has in a relatively short time. This work was funded by CMMI division of NSR, Grant No. 1728041.

REFERENCES

- Alaferdov, A. V., Savu, R., Canesqui, M. A., Kopelevich, Y. V., da Silva, R. R., Rozhkova, N. N., et al. (2018). Ripplocation in graphite nanoplatelets during sonication assisted liquid phase exfoliation. *Carbon* 129, 826–829. doi: 10.1016/j.carbon.2017.12.100
- Anasori, B., Sickafus, K. E., Usov, I. O., and Barsoum, M. W. (2011). Spherical nanoindentation study of effect of ion irradiation on deformation micromechanism of LiTaO_3 single crystals. *J. Appl. Phys.* 110:023516. doi: 10.1063/1.3608158
- Aslin, J., Mariani, E., Dawson, K., and Barsoum, M. W. (2019). Ripplocations provide a new mechanism for the deformation of phyllosilicates in the lithosphere. *Nat. Comm.* 10:686. doi: 10.1038/s41467-019-08587-2
- Asthana, A., Matsui, Y., Yasuda, M., Kimoto, K., Iwata, T., and Ohshima, K. (2005). Investigations on the structural disordering of neutron-irradiated highly oriented pyrolytic graphite by X-ray diffraction and electron microscopy. *J. Appl. Crystallogr.* 38, 361–367. doi: 10.1107/S0021889805004292
- Badr, H., Zhao, X., Koumlis, S., Tucker, G., Lamberson, L., and Barsoum, M. W. (2020). *Effect of Constraining Load and Thicknesses of Thin Steel Sheets on Their Ripplocation Mechanics*. Sub. for pub.
- Barcelo, F., Doriot, S., Cozzika, T., Le Flem, M., Béchade, J.-L., Radovic, M., et al. (2010). Electron-backscattered diffraction and transmission electron microscopy microstructural study of post-creep Ti_3SiC_2 . *J. Alloy Compds.* 488, 181–189. doi: 10.1016/j.jallcom.2009.08.073
- Barsoum, M. W., and El-Raghy, T. (1999). Room temperature ductile carbides. *Metallurg. Mater. Trans.* 30A, 363–369. doi: 10.1007/s11661-999-0325-0
- Barsoum, M. W., Farber, L., El-Raghy, T., and Levin, I. (1999). Dislocations, kink bands and room temperature plasticity of Ti_3SiC_2 . *Met. Mater. Trans.* 30A, 1727–1738. doi: 10.1007/s11661-999-0172-z

- Barsoum, M. W., Murugiah, A., Kalidindi, S. R., and Gogotsi, Y. (2004). Kink bands, nonlinear elasticity and nanoindentations in graphite. *Carbon* 42, 1435–1445. doi: 10.1016/j.carbon.2003.12.090
- Barsoum, M. W., Zhao, X., Shanazarov, S., Romanchuk, A., Koumlis, S., Pagano, S. J., et al. (2019). Ripplocations: a universal deformation mechanism in layered solids. *PR Mater.* 3:013602. doi: 10.1103/PhysRevMaterials.3.013602
- Barsoum, M. W., Zhen, T., Kalidindi, S. R., Radovic, M., and Murugiah, A. (2003). Fully reversible, dislocation-based compressive deformation of Ti_3SiC_2 to 1 GPa. *Nat. Mater.* 2, 107–111. doi: 10.1038/nmat814
- Barsoum, M. W., Zhen, T., Zhou, A., Basu, S., and Kalidindi, S. (2005). Microscale modeling of kinking nonlinear elastic solids. *Phys. Rev. B* 71:134101. doi: 10.1103/PhysRevB.71.134101
- Basu, S., and Barsoum, M. W. (2007). Deformation micromechanisms of ZnO single crystals as determined from spherical nanoindentation stress-strain curves. *J. Mater. Res.* 22, 2470–2477. doi: 10.1557/jmr.2007.0305
- Basu, S., and Barsoum, M. W. (2009). On spherical nanoindentations, kinking nonlinear elasticity of mica single crystals and their geological implications. *J. Struct. Geology* 31 791–801. doi: 10.1016/j.jsg.2009.05.008
- Basu, S., Barsoum, M. W., and Kalidindi, S. R. (2006a). Sapphire: a kinking nonlinear elastic solid. *J. Appl. Phys.* 99:063501. doi: 10.1063/1.2179974
- Basu, S., Moseson, A., and Barsoum, M. W. (2006b). On the determination of indentation stress-strain curves using spherical indenters. *J. Mater. Res.* 21, 2628–2637. doi: 10.1557/jmr.2006.0324
- Basu, S., Zhou, A. G., and Barsoum, M. W. (2008). Reversible dislocation motion under contact loading in LiNbO_3 single crystal. *J. Mater. Res.* 23, 1334–1338. doi: 10.1557/JMR.2008.0150
- Bell, I. A., and Wilson, C. J. (1981). Deformation of Biotite and Muscovite - TEM microstructure and Deformation Model *Tectonophysics* 78, 201–228. doi: 10.1016/0040-1951(81)90014-7
- Bell, I. A., Wilson, C. J. L., McLaren, A. C., and Etheridge, M. A. (1986). Kinks in mica: role of dislocations and (001) cleavage. *Tectonophysics* 127, 49–65. doi: 10.1016/0040-1951(86)90078-8
- Biot, M. A. (1964). Theory of internal buckling of a confined multilayered structure. *Geol. Soc. Am. Bull.* 75, 563–568. doi: 10.1130/0016-7606(1964)75[563:TOIBOA]2.0.CO;2
- Biot, M. A. (1965). Further development of the theory of internal buckling of multilayers. *Geol. Soc. Amer. Bull.* 76, 833–840. doi: 10.1130/0016-7606(1965)76[833:FDOTTO]2.0.CO;2
- Budd, C. J., Edmunds, R., and Hunt, G. W. (2003). Nonlinear model for parallel folding with friction. *Proc. Royal Soc. London. Seri. A*, 459, 2097–2119. doi: 10.1098/rspa.2003.1139
- Budiansky, B., Fleck, N. A., and Amazigo, J. C. (1998). On kink-band propagation in fibre composites. *J. Mech. Phys. Solids* 46, 1637–1653. doi: 10.1016/S0022-5096(97)00042-2
- Christoffersen, R., and Kronenberg, A. K. (1993). Dislocation interactions in experimentally deformed biotite. *J. Struct. Geol.* 15:1077. doi: 10.1016/0191-8141(93)90157-6
- David, E. C., Brantut, N., Schubnel, A., and Zimmerman, R. W. (2012). Sliding crack model for nonlinearity and hysteresis in the uniaxial stress-strain curve of rock. *I. J. Rock Mechan. Mining. Scien.* 52, 9–17. doi: 10.1016/j.ijrmms.2012.02.001
- Eapen, J., Krishna, R., Burchell, T. D., and Murty, K. L. (2014). Early damage mechanisms in nuclear grade graphite under irradiation. *Mater. Res. Lett.* 2, 43–50. doi: 10.1080/21663831.2013.841782
- Edmunds, R., Hicks, B. J., and Mullineux, G. (2010). Drawing parallels: modelling geological phenomena using constraint satisfaction. *J. Struct. Geol.* 32, 997–1008. doi: 10.1016/j.jsg.2010.06.005
- Edmunds, R., Hunt, G. W., and Wade, M. A. (2006). Parallel folding in multilayered structures. *J. Mech. Phys. Solids* 54, 384–400. doi: 10.1016/j.jmps.2005.08.013
- El-Raghy, T., Zavaliangos, A., Barsoum, M. W., and Kalidindi, S. R. (1997). Damage mechanisms around hardness indentations in Ti_3SiC_2 . *J. Amer. Cer. Soc.* 80, 513–516. doi: 10.1111/j.1151-2916.1997.tb02861.x
- Frank, F. C., and Stroh, A. N. (1952). On the theory of kinking. *Proc. Phys. Soc.* 65, 811–821. doi: 10.1088/0370-1301/65/10/311
- Friberg, D., Barsoum, M. W., and Tucker, G. (2018). On the nucleation of bulk ripplocations in graphite. *PRMaterials* 2:053602. doi: 10.1103/PhysRevMaterials.2.053602
- Gilbert, C. J., Bloyer, D. R., Barsoum, M. W., El-Raghy, T., Tomasia, A. P., and Ritchie, R. O. (2000). Fatigue-crack growth and fracture properties of coarse and fine-grained Ti_3SiC_2 . *Scripta Materialia* 42, 761–767. doi: 10.1016/S1359-6462(99)00427-3
- Gilman, J. J. (1954). Mechanism of ortho kink-band formation in compressed zinc monocrystals. *Trans. AIME* 200, 621–629. doi: 10.1007/BF03398884
- Griggs, J. (2016). *Investigation of the Reversible Hysteresis Effect in Hexagonal Metal Single Crystals and the MAX Phases*. Drexel University.
- Griggs, J., Lang, A., Gruber, J., Tucker, G., Taheri, M., and Barsoum, M. W. (2017). Spherical nanoindentation and transmission electron microscopy evidence for ripplocations in Ti_3SiC_2 . *Acta Mater.* 131, 141–155. doi: 10.1016/j.actamat.2017.03.055
- Gruber, J., Barsoum, M. W., and Tucker, G. J. (2020). Characterization of ripplocation mobility in graphite. *Mater. Res. Letts.* 8, 82–87. doi: 10.1080/21663831.2019.1702115
- Gruber, J., Lang, A., Griggs, J., Taheri, M., Tucker, G., and Barsoum, M. W. (2016). Evidence for bulk ripplocations in layered solids. *Sci. Rep.* 6:33451. doi: 10.1038/srep33451
- Hess, J. B., and Barrett, C. S. (1949). Structure and nature of kink bands in zinc. *Trans. AIME* 185, 599–606. doi: 10.1007/BF03398902
- Hu, C., Sakka, Y., Grasso, S., Nishimura, T., Guo, S., and Tanaka, H. (2011). Shell-like nanolayered Nb_4AlC_3 ceramic with high strength and toughness. *Scripta Mater.* 64, 765–768. doi: 10.1016/j.scriptamat.2010.12.045
- Hunt, G., Butler, R., and Budd, C. (2012). Geometry and mechanics of layered structures and materials (Theme Issue). *Phil. Trans. R. Soc. A* 370, 1723–1729. doi: 10.1098/rsta.2011.0539
- Jillson, D. C. (1950). An experimental survey of deformation and annealing processes in zinc. *Trans. AIME* 188, 1009–1018. doi: 10.1007/BF03399099
- Kabiri, Y., Schrenker, N., Julian Müller, Mirza Mačkovi, C., and Spiecker, E. (2017). Direct observation of dislocation formation and plastic anisotropy in Nb_2AlC MAX phase using in situ nanomechanics in transmission electron microscopy. *Scrip. Mater.* 137, 104–108. doi: 10.1016/j.scriptamat.2017.04.015
- Kelly, B. T. (1981). *Physics of Graphite*. London: Applied Science Publishers.
- Kooi, B. J., Poppen, R. J., Carvalho, N. J. M., and Barsoum, M. W. (2003). Ti_3SiC_2 : a damage tolerant ceramic studied with nanoindentations and transmission electron microscopy. *Acta Mater.* 51, 2859–2872. doi: 10.1016/S1359-6454(03)00091-0
- Kronenberg, A., Kirby, S., and Pinkston, J. (1990). Basal slip and mechanical anisotropy in biotite. *J. Geophys. Res.* 95:257. doi: 10.1029/JB095iB12p19257
- Kushima, A., Qian, X., Zhao, P., Zhang, S., and Li, J. (2015). Ripplocations in van der Waals Layers. *Nano Letters* 15, 1302–1308. doi: 10.1021/nl5045082
- Mares, V. M., and Kronenberg, A. K. (1993). Experimental deformation of muscovite. *J. Struct. Geol.* 15, 1061–1075. doi: 10.1016/0191-8141(93)90156-5
- Meike, A. (1989). in situ deformation of micas: a high-voltage electron-microscope study. *Am. Mineral* 74:780.
- Molina-Aldareguia, J. M., Emmerlich, J., Palmquist, J., Jansson, U., and Hultman, L. (2003). Kink formation around indents in laminated Ti_3SiC_2 thin-films studied in the nano scale. *Scripta Mater.* 49, 155–160. doi: 10.1016/S1359-6462(03)00214-8
- Moseson, A. J., Basu, S., and Barsoum, M. W. (2008). Determination of the effective zero point of contact for spherical nanoindentation. *J. Mater. Res.* 23, 204–209. doi: 10.1557/JMR.2008.0012
- Murugiah, A., Barsoum, M. W., Kalidindi, S. R., and Zhen, T. (2004). Spherical Nanoindentations in Ti_3SiC_2 . *J. Mater. Res.* 19, 1139–1148. doi: 10.1557/JMR.2004.0148
- Muto, S., and Tanabe, T. (1999). Fragmentation of graphite crystals by electron irradiation at elevated temperatures. *J. Electron Microsc.* 48, 519–523. doi: 10.1093/oxfordjournals.jmicro.a023710
- Narayanan, S., and Schadler, L. S. (1999). Mechanisms of kink-band formation in graphite/epoxy composites: a micromechanical experimental study. *Composites Sci. Tech.* 59, 2201–2213. doi: 10.1016/S0266-3538(99)00074-3
- Radovic, M., Barsoum, M. W., El-Raghy, T., Seidensticker, J., and Wiederhorn, S. M. (2000). Tensile properties of Ti_3SiC_2 in the 25–1300C temperature range. *Acta Mater.* 48:453. doi: 10.1016/S1359-6454(99)00351-1
- Savin, A. V., Korznikova, E. A., and Dmitriev, S. V. (2019). Dynamics of surface graphene ripplocations on a flat graphite substrate. *Phys. Rev. B* 99:235411. doi: 10.1103/PhysRevB.99.235411

- Shamma, M., Caspi, E., Anasori, B., Clausen, B., Brown, D., Vogel, S., et al. (2015). *in situ* neutron diffraction evidence for fully reversible dislocation motion in highly textured polycrystalline Ti₂AlC samples. *Acta Mater.* 98, 51–63. doi: 10.1016/j.actamat.2015.07.023
- Sun, Z.-M., Murugaiyah, A., Zhen, T., Zhou, A., and Barsoum, M. W. (2005). Microstructure and mechanical properties of porous Ti₃SiC₂. *Acta Mater.* 53, 4359–4366. doi: 10.1016/j.actamat.2005.05.034
- Tallman, D. J., He, L., Gan, J., Caspi, E., Hoffman, E. N., and Barsoum, M. W. (2017). Effects of neutron irradiation of Ti₃SiC₂ and Ti₃AlC₂ in the 121–1085 °C temperature range. *J. Nucl. Mater.* 484, 120–134. doi: 10.1016/j.jnucmat.2016.11.016
- Wadee, M. A., and Edmunds, R. (2005). Kink band propagation in layered structures. *J. Mech. Phys. Solids* 53, 2017–2035. doi: 10.1016/j.jmps.2005.04.005
- Wadee, M. A., Hunt, G. W., and Peletier, M. A. (2004). Kink band instability in layered structures. *J. Mech. Phys. Solids* 52, 1071–1091. doi: 10.1016/j.jmps.2003.09.026
- Walsh, J. B. (1965). The effect of cracks on the uniaxial compression of rock. *J. Geophys. Res.* 70:399. doi: 10.1029/JZ070i002p00399
- Zhen, T., Barsoum, M. W., and Kalidindi, S. R. (2005a). Effects of temperature, strain rate and grain size on the compressive properties of Ti₃SiC₂. *Acta Mat.* 53, 4163–4171. doi: 10.1016/j.actamat.2005.05.020
- Zhen, T., Barsoum, M. W., Kalidindi, S. R., Radovic, M., Sun, Z. M., and El-Raghy, T. (2005b). Compressive creep of fine and coarse-grained Ti₃SiC₂ in air in the 1100 to 1300°C temperature range. *Acta Mater.* 53, 4963–4973. doi: 10.1016/j.actamat.2005.05.037
- Zhou, A. G., Barsoum, M. W., Basu, S., Kalidindi, S. R., and El-Raghy, T. (2006). Incipient and regular kink bands in dense and 10 vol.% porous Ti₂AlC. *Acta Mat.* 54:1631e1639. doi: 10.1016/j.actamat.2005.11.035
- Zhou, A. G., Basu, B., and Barsoum, M. W. (2008). Kinking nonlinear elasticity, damping and microyielding of hexagonal close-packed metals. *Acta Mat.* 56, 60–67. doi: 10.1016/j.actamat.2007.08.050

Conflict of Interest: The author declares that the research was conducted in the absence of any commercial or financial relationships that could be construed as a potential conflict of interest.

Copyright © 2020 Barsoum. This is an open-access article distributed under the terms of the Creative Commons Attribution License (CC BY). The use, distribution or reproduction in other forums is permitted, provided the original author(s) and the copyright owner(s) are credited and that the original publication in this journal is cited, in accordance with accepted academic practice. No use, distribution or reproduction is permitted which does not comply with these terms.